Article

Calcium Carbonate Originating from Snail Shells for Synthesis of Hydroxyapatite/L-Lysine Composite: Characterization and Application to the Electroanalysis of Toluidine Blue

Jimmy Julio Kouanang Ngouoko [1], Kevin Yemele Tajeu [1,*], Cyrille Ghislain Fotsop [2], Arnaud Kamdem Tamo [3,4,5], Giscard Doungmo [6], Ranil Clément Tonleu Temgoua [1,7,*], Théophile Kamgaing [1] and Ignas Kenfack Tonle [1,*]

[1] Department of Chemistry, Faculty of Science, University of Dschang, Dschang P.O. Box 67, Cameroon
[2] Otto-von-Guericke-University Magdeburg, Chemical Institute Industrial Chemistry, Universitatsplatz 2, 39106 Magdeburg, Germany
[3] Laboratory for Bioinspired Materials BMBT, Institute of Microsystems Engineering IMTEK, University of Freiburg, 79110 Freiburg, Germany
[4] Freiburg Center for Interactive Materials and Bioinspired Technologies FIT, University of Freiburg, 79110 Freiburg, Germany
[5] Freiburg Materials Research Center FMF, University of Freiburg, 79104 Freiburg, Germany
[6] Institute of Inorganic Chemistry, Christian-Albrechts-Universitätzu Kiel, Max-Eyth-Straβe 2, 24118 Kiel, Germany
[7] Higher Teacher Training College, University of Yaoundé 1, Yaoundé P.O. Box 47, Cameroon
*   Correspondence: kevin.tajeu@univ-dschang.org (K.Y.T.); ranil.temgoua@univ-dschang.org (R.C.T.T.); ignas.tonle@univ-dschang.org (I.K.T.); Tel.: +237-697-621-152 (K.Y.T.); +237-674-413-448 (R.C.T.T.); +237-696-141-545 (I.K.T.)

Abstract: Snail shells (*Anadora Fulica*) calcined at different temperatures were characterized by X-ray diffraction (XRD), Fourier transform infrared (FTIR) spectroscopy, thermal analyses (TG-DTG), scanning electron microscopy (SEM) and N_2 adsorption–desorption experiments (surface area measurements were found using the coupled BET/BJH method). The principal objective was to identify different forms of calcium carbonate and calcium hydroxide in snail shells as raw materials. The calcium hydroxide thus obtained was used in the synthesis of the hydroxyapatite/L-lysine (HA/Lys) composite. The composite used to chemically modify a glassy carbon electrode (GCE) was characterized by cyclic voltammetry (CV) and electrochemical impedance spectroscopy (EIS). It appeared that the developed sensor Lys/HA/GCE facilitated electronic transfer compared to the pristine electrode. In a strongly acid medium, this surface protonated and therefore became positively charged, which allowed it to have a good affinity with $[Fe(CN)_6]^{3-}$. An application in toluidine blue (TB) electroanalysis in the phosphate buffer was carried out. Optimal sensor performances were obtained using cyclic voltammetry (CV) and differential pulse voltammetry (DPV). The performance of the sensor was determined in the concentration range 1 to 10 μM of TB, and the limit of detection (LOD) obtained by the S/N = 3 method was 2.78×10^{-7} M. The sensor was also used to detect the TB in spring water at 96.79% recovery.

Keywords: hydroxyapatite; electroanalysis; calcination; snail shells; toluidine blue

1. Introduction

Calcium carbonate $CaCO_3$ is an exceptional mineral that is found in large quantities in nature, rivers and oceans in different forms [1]. Among these different forms, the most important are calcite (hexagonal, space group R3c) and aragonite (orthorhombic, SG Pmcn) [2–5]. Most of these minerals are deposited in nature from rocks but also from waters, countless plants and animals [6,7]. This substance, generally used in building since the time of ancient Egypt, is today widely used in the manufacture of paper [8], plastics (polyvinyl chloride, polypropylene, polyethylene) [9], paints and coatings [10,11], in environmental

protection (desulfurization of combustion gases, neutralization of the most acidic and treatment of drinking water) and in agriculture [12].

Another particular application of calcium carbonates is the production of calcium hydroxides by calcination. Newly developed calcium hydroxides are used as a catalyst in transesterification reactions [13], the sorption of sulfur dioxide [14] and source of calcium in the synthesis of hydroxyapatites $Ca_{10}(PO_4)_6(OH)_2$ (HA) [15,16]. Synthetic HA-based compounds find several applications, e.g.: in biomedicine [17], as important bone substitutes in orthopedics and dentistry because they mimic the mineral phase of human bones and teeth [18]; in agriculture, as nanoparticles able to spread the amendments in crops [19]; in the environment, as excellent materials for water remediation [20]; in nuclear settings, as proven materials for nuclear waste storage [21]; and in cultural heritage, where they make up working films on stone monuments preserving them from weathering and acid rain [22].

These HA are usually incorporated into polymer matrices in order to increase the mechanical properties of newly synthesized materials [23]. Another particular application of this material is its use as a photoluminescent agent. Recent research, in particular that of Figuerou-Rosales et al. [24], Paterlini et al. [25] and Huerta et al. [26] showed that in the near future, HA could be used as an optoelectronic material. HA composite is a good electricity conductor [27], and therefore, in electrochemistry, it is used as an electrode modifier. In this line of thought, Tchoffo and coworkers used the composite hydroxyapatite/β-cyclodextrin for the detection of diquat herbicide and lead ions [28,29]. In this class of material, we find the composites consisting of HA and lysine. This composite is generally obtained by the absorption of L-lysine on the surface of HA [30,31]. The main objective of the fabrication of Lys/HA composite was to further increase the functional groups and active sites which allow for increased sequestration of the target analyte during the electrochemical processes involved. An important application of this new material is the electrochemical determination of synthetic dyes such as Nile blue A [32], which is part of a wide range of synthetic dyes used in medicine. In this class of dye, we also have toluidine blue (also known as tolonium chloride) which has an affinity for nucleic acids and biomolecules [33].

In the present work, we first identified and characterized (by several physicochemical and electrochemical methods) the different material forms of calcium carbonate obtained during the calcination of snail shells at different temperatures. Subsequently, we produced HA and used it to synthesize the L-lysine/hydroxyapatite (Lys/HA) composite. The composite was then characterized by electrochemical methods (EIS and CV) and used to modify the glassy carbon electrode (GCE) in order to carry out the electroanalysis of toluidine blue (dye).

2. Materials and Methods

2.1. Reagents and Chemicals

The chemicals used to conduct the experiments are as follows: Na_2HPO_4 and KH_2PO_4 (BDH Chemical Ltd., Lutterworth, UK); NaOH and EDTA (Fisher Scientific International, Hampton, New Hampshire, MA, USA); HCl (Pronalys AR, Scoresby, Australia); Nile blue A (Fischer Scientific International, 91%); L-lysine (Fisher Scientific International); citric acid monohydrate (J.T. Baker); toluidine blue (TB) (Sigma-Aldrich, Taufkirchen, Germany); methyl orange (Fisher Scientific International); ascorbic acid (Sigma-Aldrich); and $K_3Fe(CN)_6$ (>99%) (Sigma-Aldrich). For the preparation of solutions of TB at different concentrations, a stock solution (10^{-2} M) of TB was prepared in distilled water, and the dilution of this solution was performed in the phosphate buffer solution (PBS) 0.1 M at different pHs.

2.2. Procedure for Obtaining the Different Materials, Preparation of the Hydroxyapatite (HA) and Hydroxyapatite/L-Lysine (HA/Lys) Composite

Snail shells were collected with the snail meat sold by women in the town of Nkongsamba located in the Littoral region of Cameroon. The shells were cleaned with distilled water and dried at room temperature for two weeks. The snail shell calcination was obtained in an oven at increasing temperatures of 400, 700 and 1000 °C for 90 min with a temperature rise of 5 °C/min in order to follow the evolution of the crystallization of materials. The calcination temperatures used have effects on the morphology and crystalline properties of the materials obtained. Each material obtained at different temperatures was sieved to obtain only particles with a diameter less than or equal to 25 μm. The materials obtained were labeled as follows: escN (pale white powder), esc400 (grey powder), esc700 (grey powder) and esc1000 (white powder) for uncalcined and calcined materials at 400 °C, 700 °C and 1000 °C, respectively.

For the preparation of HA, 2.8 g of esc1000 were mixed with 50 mL of 0.1 M EDTA to obtain a 0.1 M Ca–EDTA complex solution. A volume of 50 mL of a 0.06 M Na_2HPO_4 was mixed at 4 mL/min, and the mixture was stirred for 120 min maintaining the pH of the mixture at around 13. A milky white powder was then obtained after drying in oven for 12 h [29]. For the preparation of the Lys/HA composite, 5 mg of L-lysine were mixed with 3 mg of hydroxyapatite in 1 mL of distilled water, and the mixture was passed through ultrasound for 30 minutes.

2.3. Characterization Techniques and Electroanalytical Methods

The synthesized HA and the composite (HA/Lys) were characterized by various physicochemical techniques.

2.3.1. X-ray Diffraction (XRD)

Ex-situ XRD data were collected using a STOE STADI P X-ray powder diffractometer (STOE and Cie GmbH, Darmstadt, Germany), with Cu $K_{\alpha 1}$ radiation (λ = 1.54056 Å; Ge monochromator; flat sample). The data were collected for the value of 2θ ranging from 5° to 70° with a scanning speed of 1.5°/min.

2.3.2. Fourier Transform Infrared (FTIR) Spectroscopy

Fourier transform infrared spectroscopy (FTIR) spectra were recorded using a genesis FTIRM spectrometer (ATI Mattson, Bremen, Germany) equipped with a DTGS (deuterated tri-glycine sulfate).

2.3.3. Thermal Analyses

Thermogravimetric analysis (TGA) and differential thermal analysis (DTA) of the powder were performed on a NETZSCH STA 449F5 thermal analyzer in air atmosphere at a heating rate of 10 °C/min up to 1000 °C (Netzsch Gerätebau GmbH, Selb, Germany).

2.3.4. Scanning Electron Microscopy (SEM)

The morphologies of the HA, Lys and Lys/HA were investigated using SEM. SEM images of dried powders were taken using a Zeiss Supra 55 VP field emission scanning electron microscope (FESEM, Carl Zeiss, Jena, Germany) at an acceleration voltage of 20 kV. Before imaging the dry powders of the samples, they were first coated with a thin gold layer under vacuum.

2.3.5. BET Analysis

Nitrogen adsorption–desorption isotherms were collected for selected samples using Sorptomatic Advanced Data Processing, Thermo electron corporation (Waltham, MA, USA). Before N_2 adsorption, the samples were degassed at 307.13 K under vacuum.

2.4. Electroanalytical Procedures

Electrochemical measurements were carried out at room temperature with μ-Autolab potentiostat (Ecochimie, Holland). The cyclic voltammograms (CV) were first recorded in the 10^{-3} M $[Fe_3(CN)_6]^{3-}$ probes containing 0.1 M NaCl. As a second step, the analysis was carried out in 0.1 M of phosphate buffer solution (PBS) containing 1 mM of TB. Optimal parameters for TB dye detection were recorded using differential pulse voltammetry (DPV). These parameters were as follows: pulse amplitude 95 mV, stop potential 7.5 mV, initial potential −0.7 V, final potential 0.2 V and equilibrium time 5 s. The initial (−0.7 V) and final (0.2 V) potentials were carefully chosen (after optimization) in order to observe the oxidation and reduction in TB (well-defined curves) in the potential range considered. The TB dye was electroactive over the wide range of potentials used (from −0.7 V to 0.2 V). The other parameters are those of the apparatus which has been used without modification. For the electroanalysis experiments, three electrodes were immersed either in one of the probes or in the PBS containing the TB dye to be analyzed.

2.5. Working Electrode Preparation Procedure

The modification of the GCE was done by drop coating. Before its surface modification, GCE was polished with alumina paste. The electrodes were then placed in a 1:1 ethanol–water solution and cleaned in an ultrasonic bath for 10 min to remove any remaining alumina particles. Finally, 5 μL of (HA or Lys or Lys/HA, depending on the case) was then deposited on the surface of the GCE and dried in an oven for one hour.

3. Results and Discussion

3.1. Characterization of the Calcium Source

The uncalcined snail shells are mainly calcium carbonates. Indeed, Figure 1a (curve 1) shows the internal vibration modes of CO_3^{2-} ions at wavenumbers of 717 cm^{-1} ($\gamma_4 CO_3^{2-}$), 857 cm^{-1} ($\gamma_2 CO_3^{2-}$), 1084 cm^{-1} ($\gamma_1 CO_3^{2-}$), 1454 cm^{-1} ($\gamma_3 CO_3^{2-}$), 1784cm^{-1} ($\gamma_3 CO_3^{2-}$) and 2521 cm^{-1} ($\gamma_1 + \gamma_3$) [30]. In agreement with Zhu and coworkers, the peaks encountered on the spectrum showed that it mainly consisted of aragonite [34]. When the calcination temperature reaches 400 °C, we find that the peak intensities on the FTIR spectra in Figure 1a (curve 2) significantly decreased. It can be considered that it is a transition phase between the aragonite and calcite that was formed. The transition to a temperature of 700 °C (curve 3) causes the disappearance of the peak at 1084 cm^{-1}, the slight displacement of the peak initially at 1454 cm^{-1} and its appearance at 1402 cm^{-1}. Other peaks appearing at 873 and 710 cm^{-1}, respectively, indicate the characteristic close to CaCO$_3$ and related to the Ca–O bond. The peaks recorded at vibration frequencies of 1402, 873 and 710 cm^{-1} are associated with the calcite form of calcium carbonate [35]. The FTIR spectrum of the material obtained after calcination at 1000 °C (Figure 1a, curve 4) highlights the characteristic peak of calcium hydroxide appearing at 3642 cm^{-1} [36]. Besides these results recorded using FTIR spectroscopy, other qualitative and quantitative information was obtained for these materials using XRD analysis. The diffractograms are exhibited in Figure 1b.

The XRD spectrum of the uncalcined shells in Figure 1b (curve 1) in comparison with XRD data already reported for CaCO$_3$ mainly shows the presence of calcium carbonate in aragonite form [37,38]. Figure 1b (curve 2) shows the XRD spectrum of esc400. Curve 2 highlights the intensity of the diminished peaks and especially, the appearance of the new peaks showing a transition phase between two different forms of calcium carbonate. The XRD pattern of the material obtained after calcining the shells at 700 °C is shown in Figure 1b (curve 3). In agreement with data reported for CaCO$_3$ (JCPDS file No. 05-0586), it can be seen that the peaks of the aragonite form have given way to a more stable form of calcium carbonate which is calcite [39]. The XRD pattern of material resulting from the calcination of the shells at 1000 °C is presented in Figure 1b (curve 4). The peaks observed on this curve match well with the reported data of CaO (JCPDS file no.48-1467), thus confirming the formation of CaO [40]. The thermal behavior of these materials has been studied through thermal analyzes, and the results obtained are presented in Figure 2.
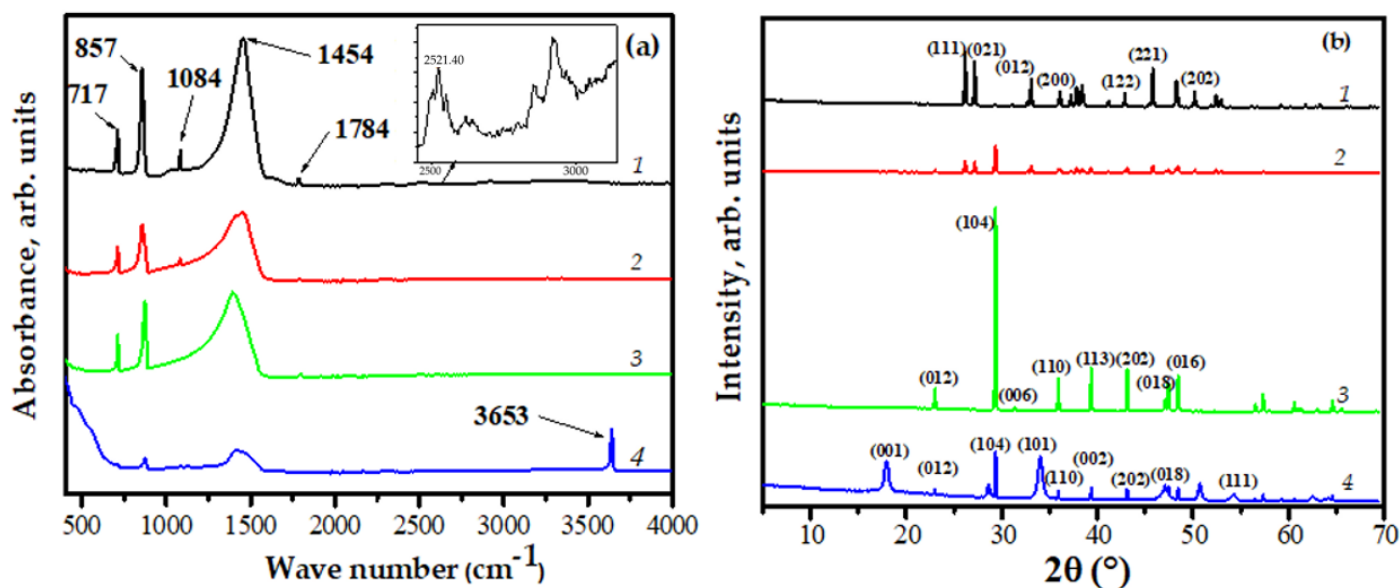
Figure 1. (**a**) FTIR spectra and (**b**) Powder X-ray diffraction patterns of (1) escN, (2) esc400, (3) esc700 and (4) esc 1000.
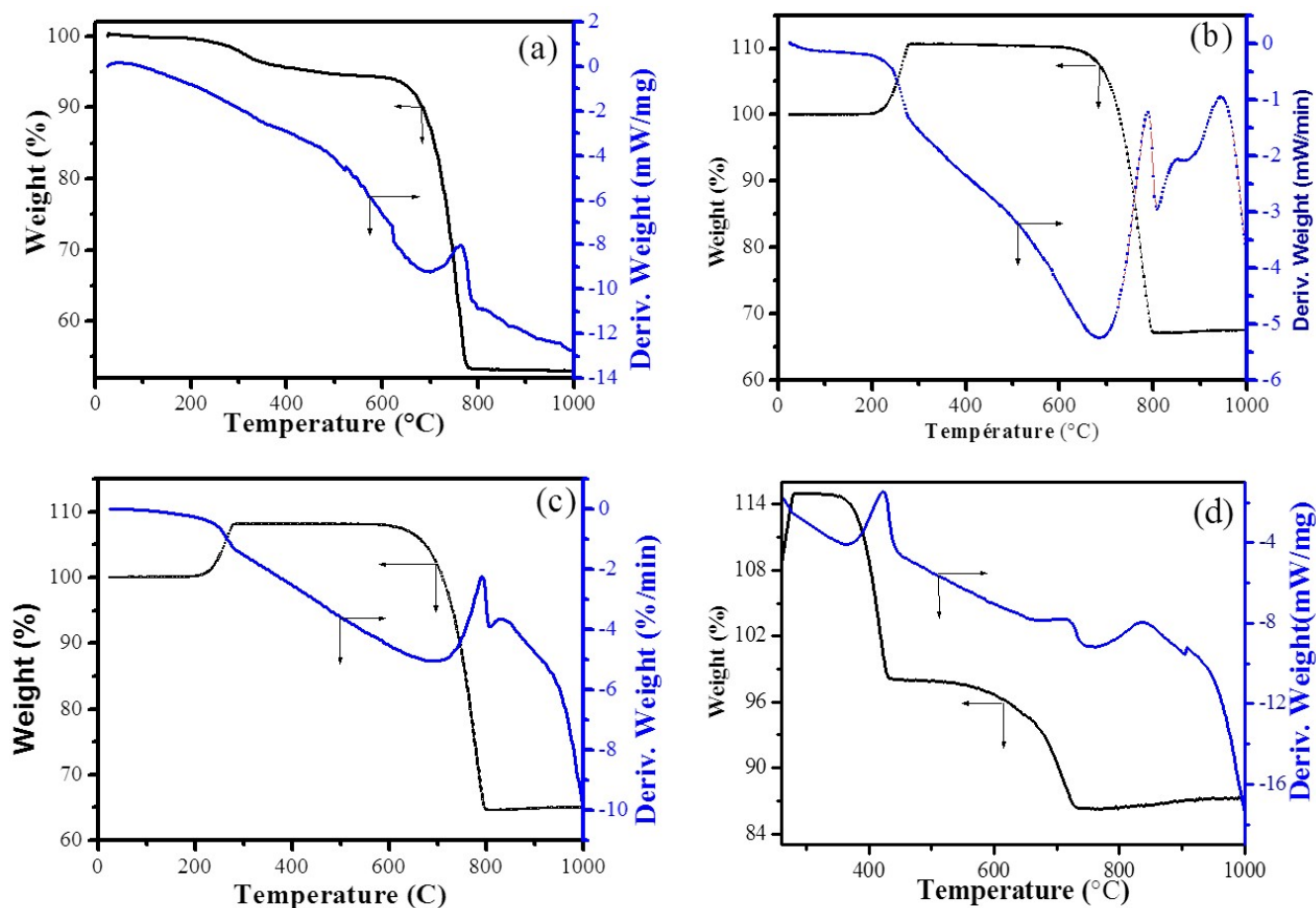

Figure 2. DTG-TG of (**a**) escN, (**b**) esc400, (**c**) esc700 and (**d**) esc1000.

Figure 2 displays the outcomes of the thermal analyzes performed on the materials escN, esc400, esc700 and esc1000. Figure 3 shows two mass losses. The first, which begins at 200 °C and ends around 540 °C, corresponds to a mass loss of around 5.5 %. The less

significant variation around 350.44 °C characterizes the endothermic nature of this process. This process is linked both to the degradation of the organic phase in the materials as well as to the transformation of the endothermic phase of aragonite into calcite. It is reported that the natural aragonite phase of the $CaCO_3$ transition temperature ranges from 450 °C to 500 °C [41]. The second mass loss begins at 600 °C and practically ends at 790 °C. This weight loss is estimated at 40% and corresponds to the total decomposition of calcium carbonate into CaO. The release of CO_2 from calcium carbonate which is an exothermic process takes place at the temperature of 740 °C [42]. The TGA curve of esc700 is displayed in Figure 3. Analyzes performed in the temperature range of 0 to 1000 °C show a one-time mass loss of approximately 43% in the temperature range of 610 to 800 °C. The DTG curve of esc700 also shows an endothermic process in the case of the escN sample. This confirms the disappearance of CO_2 during calcination, and the formation of CaO which, in the presence of atmospheric air, is transformed into $Ca(OH)_2$. As for the esc1000 sample, the curves recorded following thermal analyzes carried out on this sample are presented in Figure 2d. This figure highlights two endothermic phenomena described as follows: the first whose mass loss (16%) is between 310 and 450 °C corresponds to loss of free water inside the crystal lattice [43]; and the second mass loss of 13% between 650 and 825 °C corresponds to a decomposition of the remaining calcium carbonate and that which has formed due to the presence of CO_2 [44].
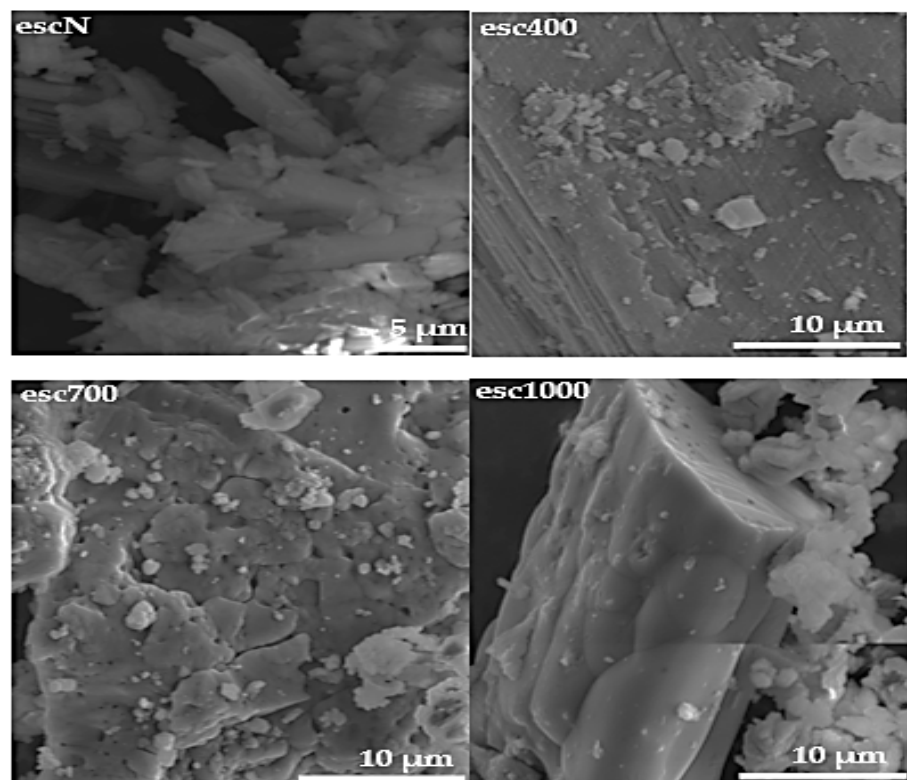

Figure 3. SEM image of escN, esc400, esc700 and esc1000.

The SEM images of the materials escN, esc400, esc700 and esc1000 are displayed in Figure 3. This analysis made it possible to follow the evolution and the change in the morphology and texture of materials impacted by the different calcination temperatures used.

In general, all materials exhibited a compact structure with a homogeneous and wrinkled surface. The particles are agglomerated in the form of platelets. In addition, SEM images highlight the crystalline character of the materials studied. The particles tend to agglomerate, and in some cases, regular stacks of chains have formed, which constitute crystalline zones or crystallites. When the temperature rises to 400 °C, the morphology of the material begins to change due to the progressive elimination of organic matter and

water contained in the matrix. The increase in the calcination temperature up to 700 °C highlights a new modification of the morphology of the material which is accompanied by a reduction in the size of its pores on the surface. The surface morphology of the esc1000 shell calcined at 1000 °C was rougher, as shown in Figure 4 for the esc1000 sample. This change in surface morphology may have resulted from a transformation of the calcite phase ($CaCO_3$) into CaO while releasing CO_2 [45].
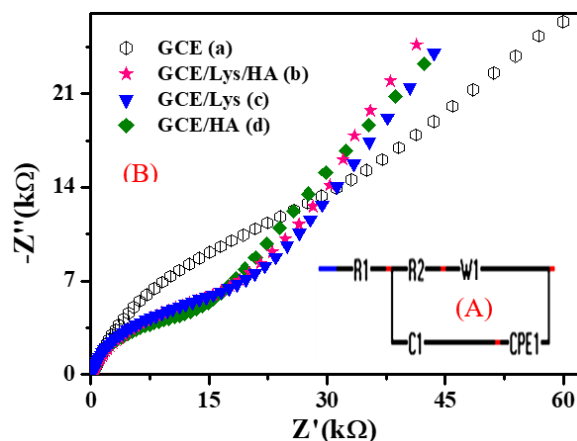

Figure 4. Nyquist EIS curves obtained on (A) the equivalent circuit; (B) (a) GCE, (b) GCE/Lys/HA, (c) GCE/Lys and (d) GCE/HA in a 0.1 M NaCl solution containing 10^{-3} M $[Fe(CN)_6]^{3-/4-}$.

The specific surface area and pore volume of the different materials were calculated using the Brunauer–Emmett–Teller (BET) and the Barrett–Joyner–Halenda (BJH) methods. The results are showed in Table 1 below.

Table 1. Specific surface area and pore volume values of materials.

Samples	Surface Area (m^2/g)	Pore Volume (cm^3/g)
escN	3.03	0.0022
esc400	2.27	0.0046
esc700	4.96	0.004
esc1000	5.22	0.0099

Table 1 above shows that, in general, the specific surface area and the pore volume increase with the increase in the calcination temperature. These results are in agreement with those found by Laskar and coworkers [41]. When the calcination temperature increases, the adsorption–desorption loop shifts to the right, causing the corresponding pore diameter and volume to increase. The steady increase in pore size as well as the decrease in particle size as the calcination temperature increases probably favors the increase in surface area and pore volume of the resulting materials.

3.2. Electrochemical Characterization of HA, Lys and Lys/HA Materials

As described in the previous section, the material obtained by calcining snail shells at a temperature of 1000 °C was used for the production of HA. To highlight the applications of this material, we used it alone or in a composite form (associating it with an essential amino acid, L-lysine (Lys), as an electrode modifier in order to improve the sensitivity and the selectivity of electrodes for the detection and quantification of target analytes in contaminated environmental media).

Figure 4 exhibits the Nyquist EIS curve of a bare glassy carbon electrode modified by HA, L-lysine and Lys/HA in 25 mL of solution containing 0.1 M NaCl and 10^{-3} mol/L of $[Fe(CN)_6]^{3-/4-}$.

From the EIS analyzer software, we realized the equivalent circuits. Therefore, the characteristics are given in Table 2 below: R_1 is the resistance of solution; R_2 is the charge

transfer resistance; W is the Warburg impedance; C_1 is the double layer capacitance at the surface of the electrode; and CPE1 is the constant phase element.

Table 2. Values taken by the different elements of each circuit.

Electrodes	C_1 (F)	R_1 (Ω)	R_2 (Ω)	W (Hz)	CPE1
GCE	0.0006	9800	15,000	2000	0.001
HA/GCE	0.0006	400	12,000	1000	0.09
Lys/GCE	0.0005	200	12,000	1000	0.09
Lys/HA/GCE	0.0005	200	9000	1950	0.0003

The charge transfer resistance was calculated when moving from one electrode to another. This value is higher on the GCE (15 kΩ), followed by Lys/GCE (12 kΩ), followed by Lys/HA/GCE (9 kΩ) and at the end of HA/GCE (12 kΩ). The results show that the electron transfer capacity at the electrode is improved when adding HA which has good electron transfer capacity. The ability of HA to transfer electrons is commonly used for electroplating [46,47]. It should be noted that compared to GCE, the charge transfer property is much better for the three materials.

In addition, the characterizations of the different materials Lys, HA and HA/Lys were also carried out in a solution containing $[Fe(CN)_6]^{3-}$ ions at a concentration of 10^{-3} M in 0.1 M KCl solution at pH 2 and pH 7. The voltammograms recorded are displayed in Figure 5 below.
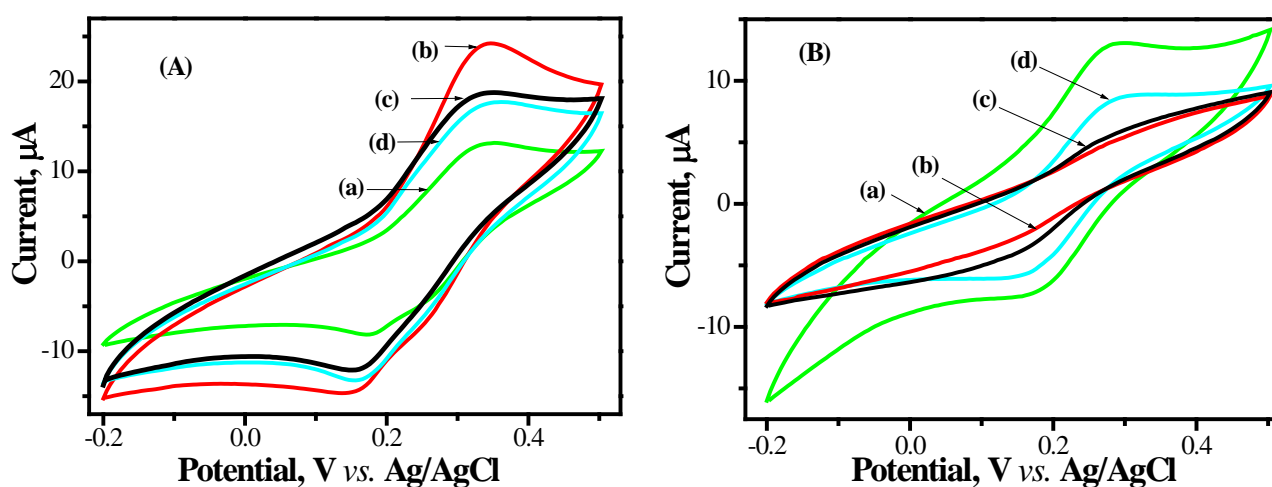

Figure 5. Cyclic voltammogram of a solution $[Fe(CN)_6]^{3-}$ 10^{-3} M after 7 scans recorded in a 0.1 M (K^+ + Cl^-) at (**A**) pH 2 and (**B**) pH 7 of (a) GCE, (b) Lys/GCE, (c) Lys/HA/GCE and (d) HA/GCE (scan rate V = 20 mV/s).

Indeed, the L-lysine group adsorbed on the surface of the HA has three pKa, 2.18, 8.95 and 10.53, respectively, associated with the $-NH_2$ and -OH groups [28]. The choice of pH 2 makes it possible to demonstrate the totally protonated character of these amine groups and to promote an interaction between the surface of the material and the analyte which is, in this case, $[Fe(CN)_6]^{3-}$ (Figure 5A). On the other hand, when using pH 7, this protonation of amino groups decreases, and the carboxylic function also loses these protons. The surface becomes progressively negatively charged, and a decrease in the intensity of the oxidation peak of the $[Fe(CN)_6]^{3-}$ ion is noted, as observed in Figure 5B. According to the analyzes carried out on this electrochemical probe $[Fe(CN)_6]^{3-}$ at two very distinct pHs (2 and 7), it can be noted that when the pH becomes lower and acidic (pH 2), the protonation of the functional groups of L-lysine (NH_3^+) leads to electrostatic interactions with negatively charged molecules in solution ($[Fe(CN)_6]^{3-}$). This is reflected in Figure 5A by the intensity of the peaks which are much higher compared to that obtained in Figure 5B

at pH 7, where the protonation is much weaker leading to less increased interaction with the negative molecules in solution.

3.3. Electrochemical Sensing of Toluidine Blue using Lys/HA Composite as Glassy Carbon Electrode Modifier

The work carried out as well as the results collected following the electroanalysis of toluidine blue on a vitreous carbon electrode modified by the Lys/HA composite film will be progressively presented in the following sections.

3.3.1. Preliminary Study on the Effect of the Working Electrode Modification with Respect to Electrochemical Detection of TB Dye

DPV curves obtained using GCE, modified, respectively, by HA (HA/GCE), Lys (GCE/Lys) and Lys/HA (Lys/HA/GCE) as modified electrodes were produced for comparison purposes with respect to the detection and quantification of TB in solution. The recorded voltammograms are shown in Figure 6 below.
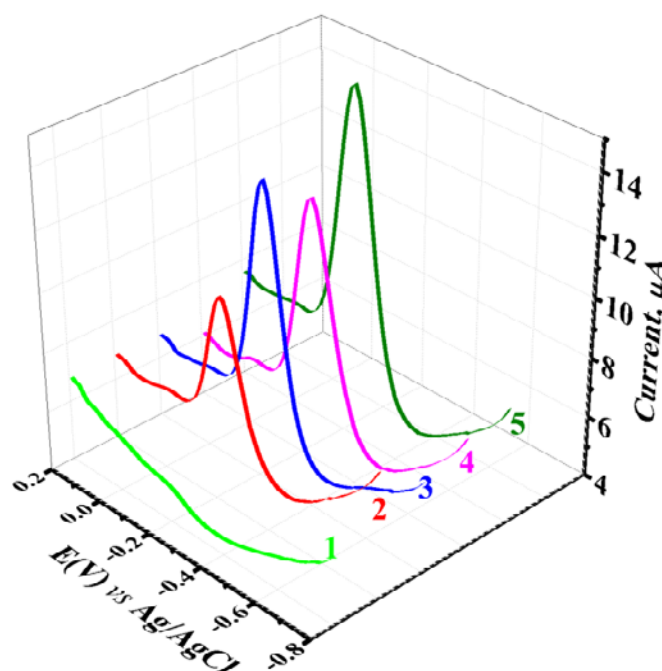

Figure 6. DPV curves obtained in 0.1 M PBS (pH 8) containing 1 μM of TB on (2) bare GCE, (3) GCE/HA, (4) GCE/Lys and (5) GCE/Lys/HA. (1) represents the curve recorded in blank electrolyte using GCE/Lys/HA.

According to these voltammograms, the most intense peak was obtained when the composite was used as modifier of the glassy carbon electrode (I_{max} = 1.556 × 10^{-5} A, E = −0.2467 V). The ratio of the intensity of this peak compared to the peaks of other materials showed, respectively, 1.12, 1.22 and 1.43 for Lys (−0.2133 V), HA (−0.2467 V) and bare GCE (−0.2318 V). From these results, we can say that the addition of the Lys/HA composite material on the surface of the electrode (Lys/HA/GCE) quantitatively improves the signal intensity. This could be due to the ability of the composite material deposited on the electrode to facilitate the electron transfer from the electrode to the analyte or from the analyte to the electrode. This is in line with the results obtained during the electrochemical characterization with the $[Fe(CN)_6]^{3-}$ ion. The electrocatalytic effect of Lys/HA on the analyte is observed because the potential on bare glassy carbon is E_{GCE} = −0.2318 V, whereas on glassy carbon modified by Lys/HA, it shows negative potentials and takes the value shown above.

3.3.2. Kinetics Studies at GCE/Lys/HA Sensor by Cyclic Voltammetry

To determine some kinetic parameters related to the redox electrochemical reaction of TB at the surface of GCE/Lys/HA, the effect of the scan rate (v) on the peak current of the oxidation and that of the reduction in TB was investigated by varying the scan rate values between 20 and 230 mV s^{-1}. Voltammograms obtained in 0.1 M PBS (pH 8) containing 1 mM TB are shown in Figure 7a.
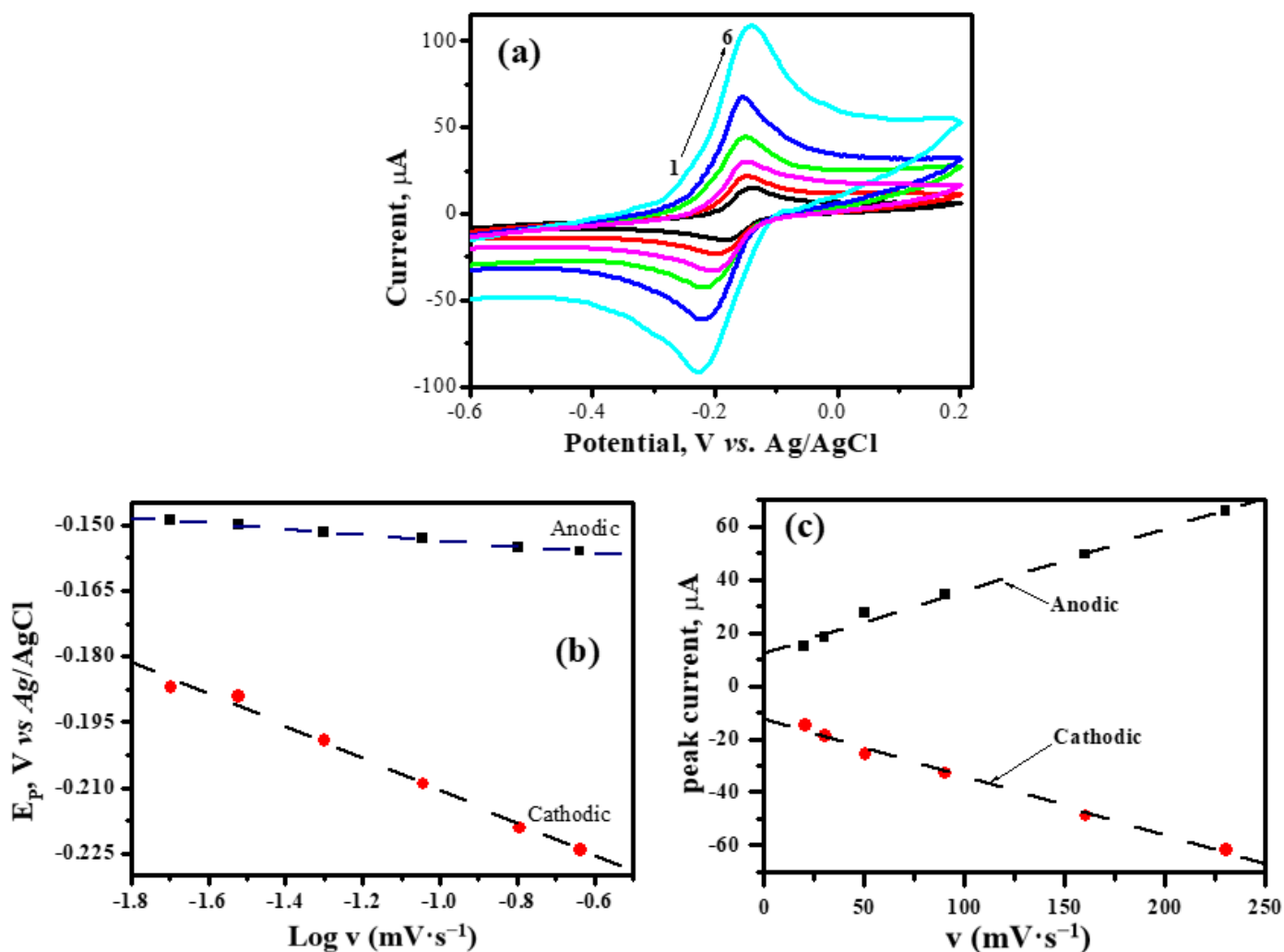

Figure 7. (**a**) Cyclic voltammograms recorded in 0.1 M PBS (at pH 8) + 1 mM TB at various scan rates: (1) 20, (2) 30, (3) 50, (4) 90, (5) 130 and (6) 230 mV s^{-1}, (**b**) Plot potential as a function of the logarithm of scan rate, (**c**) Plot of the anodic and cathodic peak currents as a function of scan rate recorded on GCE/Lys/HA.

It emerged from these investigations that the peak currents increased with the scan rate and a quasi-reversible system was recorded. The plot of peak intensity as a function of scan rate (Figure 7c) was linear. The recorded linear regression equations for oxidation and reduction in TB were, respectively:

$$I_{ox} \; (\mu A) = 0.357 \; v \; (V/s) + 0.535, \; R^2 = 0.9934 \tag{1}$$

$$I_{red} \; (\mu A) = -0.245 \; v \; (V/s) - 14.700, \; R^2 = 0.9917 \tag{2}$$

R^2 values close to 1 promote electrochemical reactions at the surface of GCE/Lys/HA essentially controlled by adsorption. Such behavior was obtained by Zeng et al. [48].

The number of electrons and the electron transfer rate constant were determined from both the plot in Figure 7b and Laviron's Equations (3) and (4) for the quasi-reversible system [49].

$$E_{pa} = E° + \left(\frac{2.303RT}{(1-\alpha)nF}\right)\log v + \left(\frac{2.303RT}{(1-\alpha)nF}\right)\log\left(\frac{nF(1-\alpha)}{RTK_s}\right) \tag{3}$$

$$E_{pc} = E° + \left(\frac{2.303RT}{\alpha nF}\right)\log v + \left(\frac{2.303RT}{\alpha nF}\right)\log\left(\frac{nF\alpha}{RTK_s}\right) \tag{4}$$

where R = 8.314 J·mol^{-1}·k^{-1}, T = 298 K and F = 96,487 C·mol^{-1}.

The value of the transfer coefficient α resulting from the slope ratio of Equations (3) and (4) is calculated from Equation (5).

$$\frac{\alpha}{1-\alpha} = \frac{0.0066}{0.0369} = 0.179 \tag{5}$$

The calculated value of α is 0.179. Reporting this in the slope of Equation (3) or Equation (4), the number of electrons transferred was found to be n = 4.57, more than four as in the literature [50]. The heterogeneous electron transfer rate constant Ks was calculated at a scan rate of 0.130 V·s^{-1} from Equation (6):

$$\log K_s = \alpha\log(1-\alpha) + (1-\alpha)\log\alpha - \log\left(\frac{RT}{nFv}\right) - \frac{\alpha(1-\alpha)nF\Delta E}{2.303RT} \tag{6}$$

A value of Ks = 0.255 s^{-1} was obtained, indicating that the electron transfer kinetics are quite fast despite the process at the electrode being quasi-reversible.

3.3.3. Effect of pH on the Peak Current and Potential

To highlight the oxidation mechanism of TB on the GCE/Lys/HA electrode, the variation of the peak potential with pH was investigated. For this purpose, DPV experiments at different pH values were performed in the PBS (Figure 8A). The plots of the peak current and peak potential versus pH are shown in Figure 8B. As noted, the current intensity increases with pH from four to six (maximum value) and then decreases from pH 6 to 7.5. Regarding the plot of the peak potential vs. pH, a linear decreasing dependent relationship was obtained, according to the equation E(V) = −0.0298 pH − 0.08281 (R^2 = 0.9999). The slope of −0.0298 V/pH obtained close to half for the theoretical value of −0.059 V/pH showed that the number of protons is equal to half the number of electrons [51]. According to the number of electrons found (four), we have two protons exchanged. The TB electro-oxidation mechanism for a unit of molecule is described according to the following Scheme 1 [51]. To be able to obtain the number of electrons exchanged according to the protons, the TB is dimerized, and the electrochemical reaction involved is presented in Scheme 2 [52].
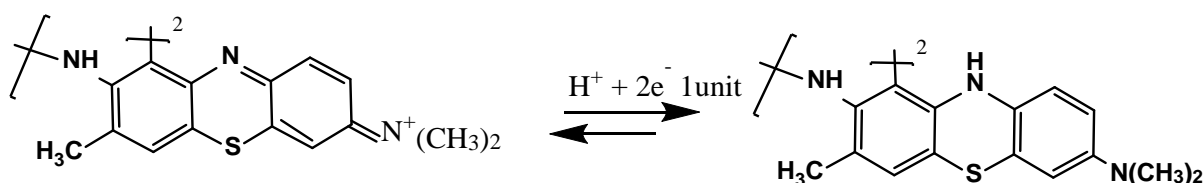
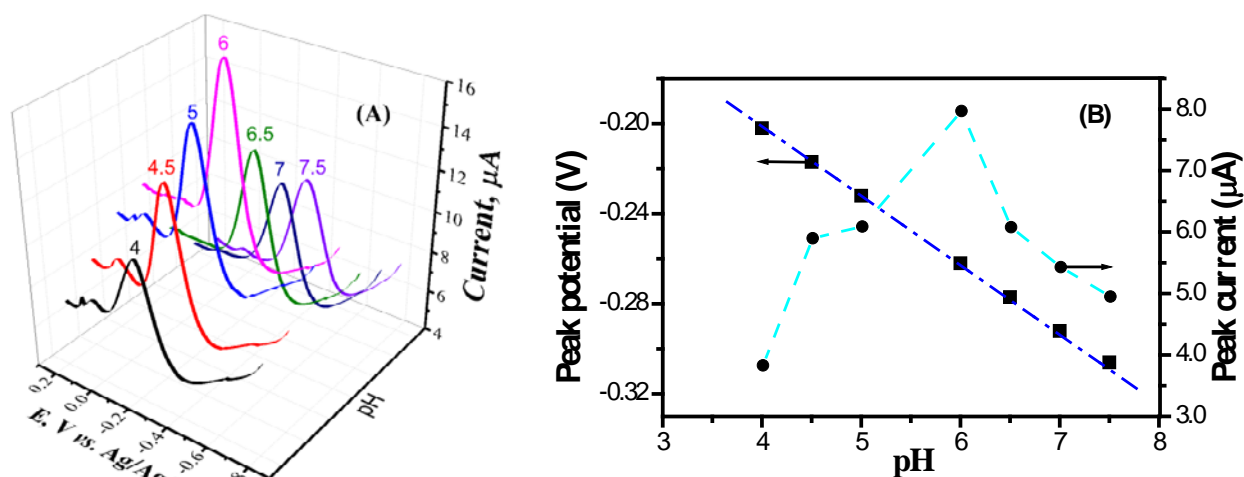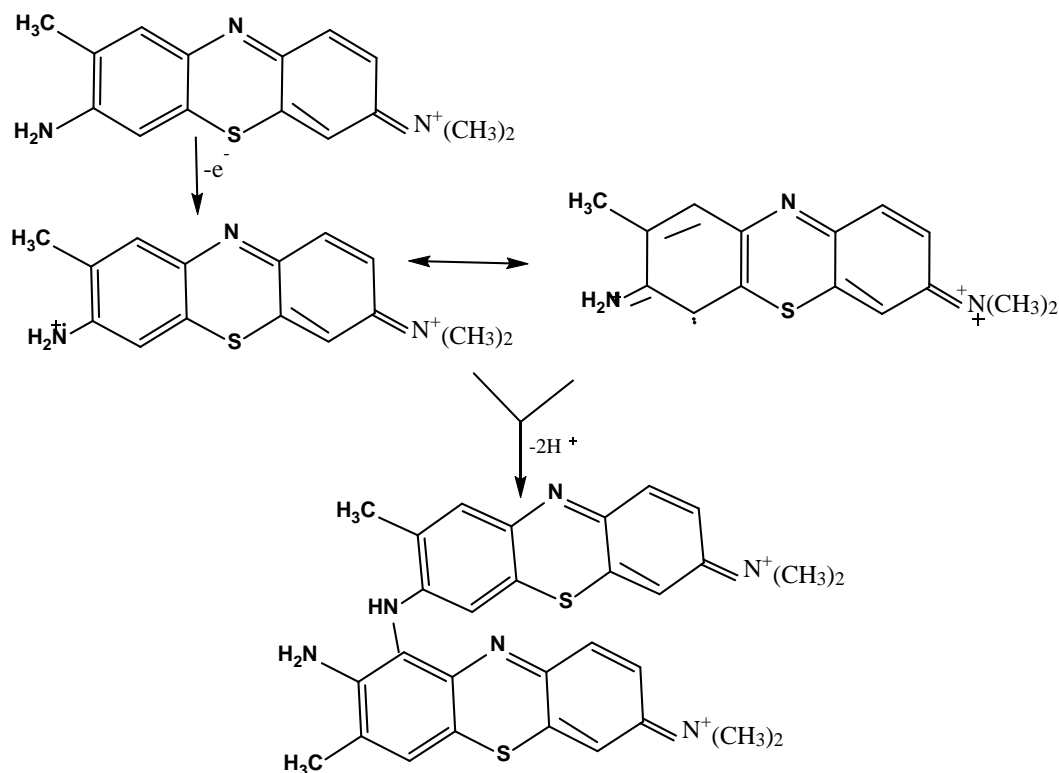**Scheme 1.** Toluidine blue electro-oxidation mechanism.

Figure 8. (A) Effect of pH of PBS solution on the peak current and peak potential of 10^{-6} M TB at GCE/Lys/HA. **(B)** The curves of i_{pa} = f (pH) and E_{pa} = f(pH).

Scheme 2. TB polymerization mechanism at the Lys/HA electrode.

3.3.4. Calibration Curve of TB Using Lys/HA/GCE as Sensor

DPV studies of TB in the concentration range of 1–10 μM were performed using GCE/Lys/HA under optimized conditions, and the recorded results are shown in Figure 9. It can be observed in the inset of Figure 9 that the peak current Ipa increases with the concentration of TB. The calibration equation and its correlation coefficient were Ipa (A) = 0.39831 [TB] (mol·L^{-1}) + 8.6554 × 10^{-8}; R^2 = 0.9979, respectively. The errors on the slope and the intercept are 0.00616 and 0.03694, respectively. The limit of detection, LOD = 2.78 × 10^{-7} mol·L^{-1}, was determined taking into account the relation 3 s/m, where s is the standard deviation on the blank, and m is the slope of the line [53]. The results obtained were the subject of a comparative study with those obtained with methylene

blue (MB) and Nile blue A (NBA), as there is no work in the literature that deals with the electroanalysis of TB dye. The results are recorded in Table 3 below.
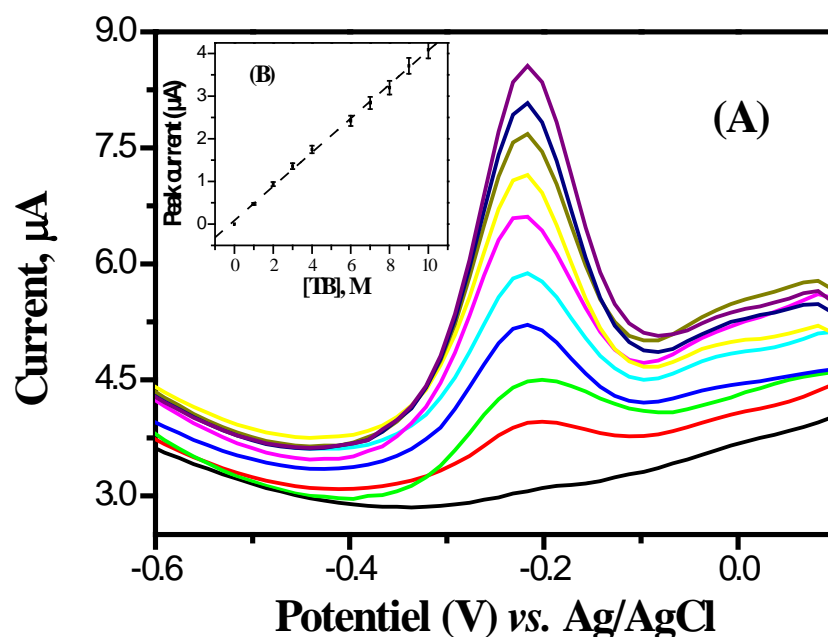

Figure 9. (A) DPV curves obtained on GCE/Lys/HA in PBS (pH 6) at different concentrations (0, 1, 2, 3, 4, 6, 7, 8, 9 and 10 μM) of TB. (B) (The inset shows the corresponding calibration curve.).

Table 3. Comparison of the detection limit of TB on the GCE/Lys/HA sensor with those obtained for other dyes analyzed by other modified electrodes.

Electrodes	Modifiers	DLR (μM)	LOD (μM)	Methods	Analytes	References
CPE [a]	Thiol functionalized-clay	1 to 14	0.4000	CV [b]	MB [c]	[54]
CPE	Ibuprofen coated gold	0.01 to 1	0.0039	DPV [d]	MB	[55]
CPE	Coffee husks	1 to 125	3.0000	SWV [e]	MB	[56]
GCE	CMTN [f]	0.01 to 10	0.0030	DPV	MB	[57]
GCE [g]	Lys/HA	0.1 to 1	0.0507	DPV	NBA [h]	[32]
GCE	Lys/HA	1 to 10	0.278	DPV	TB	This work

[a] Carbon paste electrode, CPE; [b] Cyclic voltammetry, CV; [c] Methylene blue, MB; [d] Differential pulse voltammetry, DPV; [e] Square wave voltammetry, SWV; [f] Carbon modified titanium dioxide nanostructured, CMTN; [g] Glassy carbon electrode, GCE; [h] Nile blue A, NBA.

3.3.5. Interference Studies and Analytical Application of Lys/HA Coated GCE Sensor

The interfering molecules chosen in this case to conduct this study are, respectively, Nile blue A (NBA), methyl orange (MO), iron III ion (Fe^{3+}), citric acid (CA) and oxalic acid (OA), and they are presented in the Table 4. NBA, OA and CA significantly reduce the intensity of the TB oxidation peak. The decrease in the TB oxidation peak in the presence of NBA, OA and CA could be due to a competition phenomenon of TB with each of these molecules in solution for interactions with the functional groups of the composite graft at the surface of the glassy carbon electrode. On the other hand, the Fe^{3+} and MO used increase the intensity of the anodic peak.

Table 4. Highlighting the influence of other species on the GCE/Lys/HA sensor response using TB at 5×10^{-6} mol/L TB in 0.1 M PBS pH 6.

Interference Species	Added Amount over TB Concentration	% Variation in the Anodic Peak Current of TB
NBA	2	−10.36
	4	−15.02
MO	2	+1.26
	4	+8.48
Fe^{3+}	2	+5.19
	4	+20.71
CA	2	−8.05
	4	−9.14
OA	2	−9.21
	4	−14.01

Thus, in the electrochemical cell containing a 5×10^{-6} M TB solution, the previously mentioned species were added in concentration equivalent to two- and four-fold that of TB. The peak current of TB was then recorded in optimized conditions (5 mg of Lys, 3 mg of HA, 0.1 M phosphate buffer pH 6.0) and its variations were determined and shown in Table 4.

The performance of Lys/HA as a glassy carbon electrode modifier was also highlighted in a real environment using spring water. To carry out this experiment, we took 50 mL of this water in a bottle. Previously, 25 mL of this spring water was electrochemically analyzed and showed no trace of TB. Subsequently, we introduced 6×10^{-6} M of TB in 25 mL of sampled water and recorded the voltammograms which allowed us to obtain the intensity of the maximum oxidation current for the addition (2.40×10^{-6} A). Using the equation of the calibration curve, we obtained the concentration in [TB] equal to 5.808×10^{-6} M. A recovery percentage of 96.80% was determined. Depending on the results recorded both in the real environment and on TB aqueous solutions, it can be said that the sensor developed (Lys/HA/GCE) exhibited good electroanalytical performances and can be used in particular for the detection and quantification of dyes in liquid effluents.

4. Conclusions

In this work, a source of calcium (snail shells) was identified and characterized by physicochemical techniques (FTIR, XRD, SEM, TG-DTG and N_2 adsorption–desorption). These characterizations made it possible to highlight the form of calcium carbonate present in the snail shells after calcination at different temperatures (aragonite, calcite and calcium oxide). The resulting material allowed the synthesis of the Lys/HA composite which was characterized by electrochemical methods (CV and EIS). The synthetized composite was then used for the electroanalysis of TB dye in aqueous solution. It appeared that the electrochemical redox reaction of TB at the surface of the Lys/HA/GCE modified electrode was quasi-reversible with a higher oxidation peak than those obtained when hydroxyapatite and L-lysine were individually used for the modification of the surface of the GCE. The DPV electrochemical method made it possible to determine the optimal parameters for the electroanalysis of TB dye on the Lys/HA/GCE sensor. The limit of detection obtained was 2.78×10^{-7} M, and 96.80% of this dye was detected in spring water.

Author Contributions: Conceptualization, K.Y.T., R.C.T.T., T.K. and I.K.T.; methodology, J.J.K.N. and K.Y.T.; software, J.J.K.N., K.Y.T., R.C.T.T., G.D., C.G.F. and A.K.T.; validation, T.K. and I.K.T.; formal analysis, J.J.K.N., K.Y.T., R.C.T.T., C.G.F. and A.K.T.; investigation, J.J.K.N., K.Y.T. and A.K.T.; resources, I.K.T. and T.K.; writing—original draft preparation, J.J.K.N., K.Y.T. and A.K.T.; writing— review and editing, C.G.F., A.K.T., R.C.T.T. and I.K.T.; supervision, K.Y.T. and I.K.T.; project administration, I.K.T.; funding acquisition, I.K.T. All authors have read and agreed to the published version of the manuscript.

References

1. Deng, H.; Shen, X.-C.; Wang, X.-M.; Du, C. Calcium carbonate crystallization controlled by functional groups: A mini-review. *Front. Mater. Sci.* **2013**, *7*, 62–68. [CrossRef]
2. Gavryushkin, P.N.; Belonoshko, A.B.; Sagatov, N.; Sagatova, D.; Zhitova, E.; Krzhizhanovskaya, M.G.; Rečnik, A.; Alexandrov, E.V.; Medrish, I.V.; Popov, Z.I.; et al. Metastable structures of CaCO 3 and their role in transformation of calcite to aragonite and postaragonite. *Cryst. Growth Des.* **2021**, *21*, 65–74. [CrossRef]
3. Caspi, E.N.; Pokroy, B.; Lee, P.L.; Quintana, J.P.; Zolotoyabko, E. On the structure of aragonite. *Acta Crystallogr. B* **2005**, *61*, 129–132. [CrossRef]
4. Falini, G.; Fermani, S.; Vanzo, S.; Miletic, M.; Zaffino, G. Influence on the Formation of Aragonite or Vaterite by Otolith Macromolecules. *Eur. J. Inorg. Chem.* **2005**, *2005*, 162–167. [CrossRef]
5. Gopi, S.; Subramanian, V.K.; Palanisamy, K. Aragonite–calcite–vaterite: A temperature influenced sequential polymorphic transformation of CaCO3 in the presence of DTPA. *Mater. Res. Bull.* **2013**, *48*, 1906–1912. [CrossRef]
6. Gower, L.B. Biomimetic model systems for investigating the amorphous precursor pathway and its role in biomineralization. *Chem. Rev.* **2008**, *108*, 4551–4627. [CrossRef]
7. Ni, M.; Ratner, B.D. Differentiation of Calcium Carbonate Polymorphs by Surface Analysis Techniques—An XPS and TOF-SIMS study. *Surf. Interface Anal.* **2008**, *40*, 1356–1361. [CrossRef]
8. Pöykiö, R.; Nurmesniemi, H. Calcium carbonate waste from an integrated pulp and paper mill as a potential liming agent. *Environ. Chem. Lett.* **2008**, *6*, 47–51. [CrossRef]
9. Srivabut, C.; Ratanawilai, T.; Hiziroglu, S. Statistical modeling and response surface optimization on natural weathering of wood–plastic composites with calcium carbonate filler. *J. Mater. Cycles Waste Manag.* **2021**, *23*, 1503–1517. [CrossRef]
10. Zhang, H.; Zeng, X.; Gao, Y.; Shi, F.; Zhang, P.; Chen, J.-F. A Facile Method To Prepare Superhydrophobic Coatings by Calcium Carbonate. *Ind. Eng. Chem. Res.* **2011**, *50*, 3089–3094. [CrossRef]
11. Ersoy, O.; Güler, D.; Rençberoğlu, M. Effects of Grinding Aids Used in Grinding Calcium Carbonate (CaCO3) Filler on the Properties of Water-Based Interior Paints. *Coatings* **2022**, *12*, 44. [CrossRef]
12. Schreiber, M.; Nunez, G. Calcium Carbonate Can Be Used to Manage Soilless Substrate pH for Blueberry Production. *Horticulturae* **2021**, *7*, 74. [CrossRef]
13. Kouzu, M.; Kasuno, T.; Tajika, M.; Sugimoto, Y.; Yamanaka, S.; Hidaka, J. Calcium oxide as a solid base catalyst for transesterification of soybean oil and its application to biodiesel production. *Fuel* **2008**, *87*, 2798–2806. [CrossRef]
14. He, K.; Song, Q.; Yan, Z.; Zheng, N.; Yao, Q. Study on competitive absorption of SO_3 and SO_2 by calcium hydroxide. *Fuel* **2019**, *242*, 355–361. [CrossRef]
15. Pham Minh, D.; Lyczko, N.; Sebei, H.; Nzihou, A.; Sharrock, P. Synthesis of calcium hydroxyapatite from calcium carbonate and different orthophosphate sources: A comparative study. *Mater. Sci. Eng. B* **2012**, *177*, 1080–1089. [CrossRef]
16. Pham Minh, D.; Tran, N.D.; Nzihou, A.; Sharrock, P. One-Step Synthesis of Calcium Hydroxyapatite from Calcium Carbonate and Orthophosphoric Acid under Moderate Conditions. *Ind. Eng. Chem. Res.* **2013**, *52*, 1439–1447. [CrossRef]
17. Fiume, E.; Magnaterra, G.; Rahdar, A.; Verné, E.; Baino, F. Hydroxyapatite for Biomedical Applications: A Short Overview. *Ceramics* **2021**, *4*, 542–563. [CrossRef]
18. Singh, G.; Singh, R.P.; Jolly, S.S. Customized hydroxyapatites for bone-tissue engineering and drug delivery applications: A review. *J. Sol-Gel Sci. Technol.* **2020**, *94*, 505–530. [CrossRef]
19. Yoon, H.Y.; Lee, J.G.; Degli Esposti, L.; Iafisco, M.; Kim, P.J.; Shin, S.G.; Jeon, J.-R.; Adamiano, A. Synergistic Release of Crop Nutrients and Stimulants from Hydroxyapatite Nanoparticles Functionalized with Humic Substances: Toward a Multifunctional Nanofertilizer. *ACS Omega* **2020**, *5*, 6598–6610. [CrossRef]
20. Koliyabandara, P.A.; Hettithanthri, O.; Rathnayake, A.; Rajapaksha, A.U.; Nanayakkara, N.; Vithanage, M. Hydroxyapatite for environmental remediation of water/wastewater. In *Integrated Environmental Technologies for Wastewater Treatment and Sustainable Development*; Elsevier: Alpharetta, GA, USA, 2022; pp. 167–191, ISBN 9780323911801.
21. Tran, T.N.; Kim, J.; Park, J.-S.; Chung, Y.; Han, J.; Oh, S.; Kang, S. Novel Hydroxyapatite Beads for the Adsorption of Radionuclides from Decommissioned Nuclear Power Plant Sites. *Appl. Sci.* **2021**, *11*, 1746. [CrossRef]
22. Capitelli, F.; Dida, B.; Della Ventura, G.; Baldassarre, F.; Capelli, D.; Senesi, G.S.; Mele, A.; Siliqi, D. Functional Nano-Hydroxyapatite for Applications in Conservation of Stony Monuments of Cultural Heritage. In *The 2nd International Online Conference on Crystals*; International Online Conference on Crystals; MDPI: Basel, Switzerland, 2020; pp. 1–12.
23. Guo, N.; Zhao, M.; Li, S.; Hao, J.; Wu, Z.; Zhang, C. Stereocomplexation Reinforced High Strength Poly(L-lactide)/Nanohydroxyapatite Composites for Potential Bone Repair Applications. *Polymers* **2022**, *14*, 645. [CrossRef]

24. Figueroa-Rosales, E.X.; Martínez-Juárez, J.; García-Díaz, E.; Hernández-Cruz, D.; Sabinas-Hernández, S.A.; Robles-Águila, M.J. Photoluminescent Properties of Hydroxyapatite and Hydroxyapatite/Multi-Walled Carbon Nanotube Composites. *Crystals* **2021**, *11*, 832. [CrossRef]

25. Paterlini, V.; Bettinelli, M.; Rizzi, R.; El Khouri, A.; Rossi, M.; Della Ventura, G.; Capitelli, F. Characterization and Luminescence of Eu3+- and Gd3+-Doped Hydroxyapatite $Ca_{10}(PO_4)_6(OH)_2$. *Crystals* **2020**, *10*, 806. [CrossRef]

26. Huerta, V.J.; Fernández, P.; Gómez, V.; Graeve, O.A.; Herrera, M. Defect-related luminescence properties of hydroxyapatite nanobelts. *Appl. Mater. Today* **2020**, *21*, 100822. [CrossRef]

27. Marincaș, L.; Turdean, G.L.; Toșa, M.; Kovács, Z.; Kovács, B.; Barabás, R.; Farkas, N.-I.; Bizo, L. Hydroxyapatite and Silicon-Modified Hydroxyapatite as Drug Carriers for 4-Aminopyridine. *Crystals* **2021**, *11*, 1124. [CrossRef]

28. Tchoffo, R.; Ngassa, G.B.P.; Doungmo, G.; Kamdem, A.T.; Tonlé, I.K.; Ngameni, E. Surface functionalization of natural hydroxyapatite by polymerization of β-cyclodextrin: Application as electrode material for the electrochemical detection of Pb(II). *Environ. Sci. Pollut. Res. Int.* **2022**, *29*, 222–235. [CrossRef]

29. Tchoffo, R.; Ngassa, G.B.P.; Tonlé, I.K.; Ngameni, E. Electroanalysis of diquat using a glassy carbon electrode modified with natural hydroxyapatite and β-cyclodextrin composite. *Talanta* **2021**, *222*, 121550. [CrossRef]

30. Lou, Z.; Zeng, Q.; Chu, X.; Yang, F.; He, D.; Yang, M.; Xiang, M.; Zhang, X.; Fan, H. First-principles study of the adsorption of lysine on hydroxyapatite (100) surface. *Appl. Surf. Sci.* **2012**, *258*, 4911–4916. [CrossRef]

31. Koutsopoulos; Dalas. The Crystallization of Hydroxyapatite in the Presence of Lysine. *J. Colloid Interface Sci.* **2000**, *231*, 207–212. [CrossRef]

32. Ngouoko, J.J.K.; Tajeu, K.Y.; Temgoua, R.C.T.; Doungmo, G.; Doench, I.; Tamo, A.K.; Kamgaing, T.; Osorio-Madrazo, A.; Tonle, I.K. Hydroxyapatite/L-Lysine Composite Coating as Glassy Carbon Electrode Modifier for the Analysis and Detection of Nile Blue A. *Materials* **2022**, *15*, 4626. [CrossRef]

33. Sridharan, G.; Shankar, A.A. Toluidine blue: A review of its chemistry and clinical utility. *J. Oral Maxillofac. Pathol.* **2012**, *16*, 251–255. [CrossRef]

34. Comeau, P.; Willett, T. Impact of Side Chain Polarity on Non-Stoichiometric Nano-Hydroxyapatite Surface Functionalization with Amino Acids. *Sci. Rep.* **2018**, *8*, 12700. [CrossRef]

35. Cai, G.-B.; Chen, S.-F.; Liu, L.; Jiang, J.; Yao, H.-B.; Xu, A.-W.; Yu, S.-H. 1,3-Diamino-2-hydroxypropane-N,N,N′,N′-tetraacetic acid stabilized amorphous calcium carbonate: Nucleation, transformation and crystal growth. *CrystEngComm* **2010**, *12*, 234–241. [CrossRef]

36. Lee, Y.-L.; Wang, W.-H.; Lin, F.-H.; Lin, C.-P. Hydration behaviors of calcium silicate-based biomaterials. *J. Formos. Med. Assoc.* **2017**, *116*, 424–431. [CrossRef]

37. Gao, J.; Liu, Y.; Wu, X.; Yuan, X.; Liu, Y.; Su, W. Structural Modifications of Single-Crystal Aragonite $CaCO_3$ Beginning at ~15 GPa: In Situ Vibrational Spectroscopy and X-Ray Diffraction Evidence. *Minerals* **2020**, *10*, 924. [CrossRef]

38. Kontoyannis, C.G.; Vagenas, N.V. Calcium carbonate phase analysis using XRD and FT-Raman spectroscopy. *Analyst* **2000**, *125*, 251–255. [CrossRef]

39. LABIDI, N.S.; DJEBAILI, A. Studies of The Mechanism of Polyvinyl Alcohol Adsorption on The Calcite/Water Interface in The Presence of Sodium Oleate. *JMMCE* **2008**, *07*, 147–161. [CrossRef]

40. Poralan, G.M.; Gambe, J.E.; Alcantara, E.M.; Vequizo, R.M. X-ray diffraction and infrared spectroscopy analyses on the crystallinity of engineered biological hydroxyapatite for medical application. *IOP Conf. Ser. Mater. Sci. Eng.* **2015**, *79*, 12028. [CrossRef]

41. Laskar, I.B.; Rajkumari, K.; Gupta, R.; Chatterjee, S.; Paul, B.; Rokhum, S.L. Waste snail shell derived heterogeneous catalyst for biodiesel production by the transesterification of soybean oil. *RSC Adv.* **2018**, *8*, 20131–20142. [CrossRef]

42. Labus, K. Comparison of the Properties of Natural Sorbents for the Calcium Looping Process. *Materials* **2021**, *14*, 548. [CrossRef]

43. Zhang, G.; Xu, J. From colloidal nanoparticles to a single crystal: New insights into the formation of nacre's aragonite tablets. *J. Struct. Biol.* **2013**, *182*, 36–43. [CrossRef]

44. An, Y.; Liu, Z.; Wu, W. Phase transition of aragonite in abalone nacre. *Phase Transit.* **2013**, *86*, 391–395. [CrossRef]

45. Baumer, A.; Ganteaume, M.; Bernat, M. Variations de la teneur en eau des coraux lors de la transformation aragonite → calcite. *Thermochim. Acta* **1993**, *221*, 255–262. [CrossRef]

46. Geuli, O.; Lewinstein, I.; Mandler, D. Composition-Tailoring of ZnO-Hydroxyapatite Nanocomposite as Bioactive and Antibacterial Coating. *ACS Appl. Nano Mater.* **2019**, *2*, 2946–2957. [CrossRef]

47. Chen, S.-H.; Tsai, W.-L.; Chen, P.-C.; Fang, A.; Say, W.-C. Influence of Applied Voltages on Mechanical Properties and In-Vitro Performances of Electroplated Hydroxyapatite Coatings on Pure Titanium. *J. Electrochem. Soc.* **2016**, *163*, D305–D308. [CrossRef]

48. Zeng, J.; Wei, W.; Wu, L.; Liu, X.; Liu, K.; Li, Y. Fabrication of poly(toluidine blue O)/carbon nanotube composite nanowires and its stable low-potential detection of NADH. *J. Electroanal. Chem.* **2006**, *595*, 152–160. [CrossRef]

49. Laviron, E. General expression of the linear potential sweep voltammogram in the case of diffusionless electrochemical systems. *J. Electroanal. Chem. Interfacial Electrochem.* **1979**, *101*, 19–28. [CrossRef]

50. Zhou, D.-m.; Sun, J.-J.; Chen, H.-y.; Fang, H.-q. Electrochemical polymerization of toluidine blue and its application for the amperometric determination of β-d-glucose. *Electrochim. Acta* **1998**, *43*, 1803–1809. [CrossRef]

51. Nasri, Z.; Shams, E.; Ahmadi, M. Direct Modification of a Glassy Carbon Electrode with Toluidine Blue Diazonium Salt: Application to NADH Determination and Biosensing of Ethanol. *Electroanalysis* **2013**, *25*, 1917–1925. [CrossRef]

52. Cai, C.-X.; Xue, K.-H. Electrochemical polymerization of toluidine blue o and its electrocatalytic activity toward NADH oxidation. *Talanta* **1998**, *47*, 1107–1119. [CrossRef]

53. Tajeu, K.Y.; Ymele, E.; Zambou Jiokeng, S.L.; Tonle, I.K. Electrochemical Sensor for Caffeine Based on a Glassy Carbon Electrode Modified with an Attapulgite/nafion Film. *Electroanalysis* **2018**, *6*, 997. [CrossRef]

54. Tonlé, I.K.; Ngameni, E.; Tcheumi, H.L.; Tchiéda, V.; Carteret, C.; Walcarius, A. Sorption of methylene blue on an organoclay bearing thiol groups and application to electrochemical sensing of the dye. *Talanta* **2008**, *74*, 489–497. [CrossRef]

55. Hassan, S.S.; Nafady, A.; Sirajuddin; Solangi, A.R.; Kalhoro, M.S.; Abro, M.I.; Sherazi, S.T.H. Ultra-trace level electrochemical sensor for methylene blue dye based on nafion stabilized ibuprofen derived gold nanoparticles. *Sens. Actuators B Chem.* **2015**, *208*, 320–326. [CrossRef]

56. Njanja, E.; Mbokou, S.F.; Pontie, M.; Nacef, M.; Tonle, I.K. Comparative assessment of methylene blue biosorption using coffee husks and corn cobs: Towards the elaboration of a lignocellulosic-based amperometric sensor. *SN Appl. Sci.* **2019**, *1*, 233. [CrossRef]

57. Nekoueian, K.; Jafari, S.; Amiri, M.; Sillanpaa, M. Pre-Adsorbed Methylene Blue at Carbon-Modified TiO_2 Electrode: Application for Lead Sensing in Water. *IEEE Sens. J.* **2018**, *18*, 9477–9485. [CrossRef]